

 Open access • Journal Article • DOI:10.1038/NATURE08234

A tunable topological insulator in the spin helical Dirac transport regime

— [Source link](#) 

David Hsieh, Yuqi Xia, Dong Qian, Lewis Wray ...+15 more authors

Institutions: Princeton University, Shanghai Jiao Tong University, Paul Scherrer Institute, University of Zurich ...+2 more institutions

Published on: 27 Aug 2009 - Nature (Nature Publishing Group)

Topics: Dirac fermion, Helical Dirac fermion, Topological insulator, Topological order and Topological quantum number

Related papers:

- [Colloquium: Topological insulators](#)
- [Topological insulators in Bi₂Se₃, Bi₂Te₃ and Sb₂Te₃ with a single Dirac cone on the surface](#)
- [Observation of a large-gap topological-insulator class with a single Dirac cone on the surface](#)
- [Experimental realization of a three-dimensional topological insulator, Bi₂Te₃](#)
- [Topological insulators and superconductors](#)

Share this paper:    

View more about this paper here: <https://typeset.io/papers/a-tunable-topological-insulator-in-the-spin-helical-dirac-40ub5apcre>



University of Zurich
Zurich Open Repository and Archive

Winterthurerstr. 190
CH-8057 Zurich
<http://www.zora.uzh.ch>

Year: 2009

A tunable topological insulator in the spin helical Dirac transport regime

Hsieh, D; Xia, Y; Qian, D; Wray, L; Dil, J H; Meier, F; Osterwalder, J; Patthey, L;
Checkelsky, J G; Ong, N P; Fedorov, A V; Lin, H; Bansil, A; Grauer, D; Hor, Y S;
Cava, R J; Hasan, M Z

Hsieh, D; Xia, Y; Qian, D; Wray, L; Dil, J H; Meier, F; Osterwalder, J; Patthey, L; Checkelsky, J G; Ong, N P; Fedorov, A V; Lin, H; Bansil, A; Grauer, D; Hor, Y S; Cava, R J; Hasan, M Z (2009). A tunable topological insulator in the spin helical Dirac transport regime. *Nature*, 460(7259):1101-1105.

Postprint available at:
<http://www.zora.uzh.ch>

Posted at the Zurich Open Repository and Archive, University of Zurich.
<http://www.zora.uzh.ch>

Originally published at:
Nature 2009, 460(7259):1101-1105.

A tuneable topological insulator in the spin helical Dirac transport regime

D. Hsieh¹, Y. Xia¹, D. Qian¹, L. Wray¹, J. H. Dil^{2,3}, F. Meier^{2,3}, J. Osterwalder³, L. Patthey², J. G. Checkelsky¹, N. P. Ong¹, A. V. Fedorov⁴, H. Lin⁵, A. Bansil⁵, D. Grauer⁶, Y. S. Hor⁶, R. J. Cava⁶ and M. Z. Hasan^{1,7}

¹ *Joseph Henry Laboratories of Physics, Department of Physics, Princeton University, Princeton, NJ 08544, USA*

² *Swiss Light Source, Paul Scherrer Institute, CH-5232, Villigen, Switzerland*

³ *Physik-Institute, Universitat Zurich-Irchel, 8057 Zurich, Switzerland*

⁴ *Advanced Light Source, Lawrence Berkeley Laboratory, Berkeley, CA 94720, USA*

⁵ *Department of Physics, Northeastern University, Boston, MA 02115, USA*

⁶ *Department of Chemistry, Princeton University, Princeton, NJ 08544, USA*

⁷ *Princeton Center for Complex Materials, School of Engineering and Applied Sciences, Princeton University, Princeton, NJ 08544, USA*

The manipulation of atomic spin-orbit coupling to simulate the effect of a spin dependent magnetic field in condensed matter systems has recently emerged as a route to exotic spin-phases of matter that comprise fundamentally new constituent particles¹. Recently there is heightened interest in finding a particularly elusive particle that is the unpaired helical Dirac fermion. This is a charge carrier whose dynamics mimic that of light but has a quantum spin polarization that is one-to-one locked to its direction of motion, a phenomenon forbidden to exist in ordinary Dirac materials such as graphene² or bismuth^{3,4}. It has been proposed that ensembles of such helical Dirac fermions may exist at the edges of certain types of

topologically ordered insulators, which can exhibit novel quantum entangled behaviours provided the system is tuned into a topological transport regime⁵⁻¹². However, helical Dirac fermions have not been observed in existing topological insulators¹³⁻¹⁷ to date because conventional electrical gating based tuning techniques needed^{2,18} cannot be applied on the surface and the necessary spin-sensitive detections are lacking. Here we report the first realization of a tuneable topological insulator based on the Bi_2X_3 ($\text{X}=\text{Se}, \text{Te}$)-class by combining spin- and momentum-resolved spectroscopies, bulk charge compensation and surface control. Our results reveal a helical Dirac cone that is nearly 100% spin-polarized, which exhibits a tuneable topological fermion density in the vicinity of the Kramers' point and can be driven to the long-sought topological transport regime. The observed Kramers' nodal Dirac ground state is found to be protected even up to room temperature. Taken collectively, these results show that a spin-polarized version of relativistic electrons is realized on the edge of $\text{Bi}_{2-x}\text{Ca}_x\text{Se}_3$, allowing experimental access to and device incorporation of the topological helical fermion for the first time.

Considerable attention has focused on the electrical and spin behaviors of topological helical fermions, which have long been predicted to obey unusual physical laws such as exotic electrodynamics^{7,10,11,19} and particle exchange statistics that differs from the conventional Bose or Fermi-Dirac statistics^{8,9}. Helical fermions are believed to exist on the edges of certain types of three-dimensional (3D) topological insulators^{5,6}, with several material candidates recently proposed based on observations^{14,17} and models^{20,21}. However, these materials cannot be used to detect helical Dirac fermion physics for three reasons: First, the helical properties of the surface electrons are unknown and depends on the materials class. Second, their electronic structure is not in the topological transport regime, thus not allowing any of the interesting topological insulator experiments to be performed. And third, unlike 2D Dirac quantum Hall

systems such as graphene^{2,18}, 3D topological insulators cannot be tuned to this regime through electrical gating, which has prevented a revolution like that witnessed for graphene² from taking place for topological insulators.

To determine the key helical properties of the surface electrons near the Fermi level (E_F) in the candidate Bi_2X_3 class, we performed spin- and angle-resolved photoemission spectroscopy (ARPES) scans using a double Mott detector setup²², which systematically measures all *three* components of the spin vector of a photoelectron as a function of its energy and momentum throughout the Brillouin zone (SI). Although the surface electrons of both Bi_2Se_3 and Bi_2Te_3 exhibit a finite density of states near E_F (Figs 1(a)-(d)), there is an additional contribution to the density of states around momentum $\bar{\Gamma}$ from the spin-degenerate bulk conduction band in Bi_2Se_3 ¹⁴. Therefore, the helical nature of the surface electrons is most clearly resolved in Bi_2Te_3 (SI). We analyzed the spin-polarization of photoelectrons emitted at a binding energy $E_B = -20$ meV along the k_x ($\parallel \bar{\Gamma} - \bar{M}$) cut in Bi_2Te_3 (inset Fig. 1(e)). Because the surface state dispersion of Bi_2X_3 exhibits a pronounced time dependence after cleavage (SI) related to semiconductor band bending effects¹⁶, data collection times were only long enough to ensure a level of statistics sufficient to measure the spin-polarized character of the surface states. Figures 1(e) and (f) show the measured spin polarization spectra P_i of the $i = x, y$ and z (out-of-plane) components along the $\bar{\Gamma} - \bar{M}$ direction. In the x and z directions, no clear signal can be discerned within the margins of statistical error. In the y direction on the other hand, clear polarization signals of equal magnitude and opposite sign are observed for surface electrons of opposite momentum, evidence that the spin and momentum directions are one-to-one locked. This is most clearly seen in the spin-resolved spectra ($I_y^{\uparrow,\downarrow}$) (Fig. 1(g)), which are calculated from P_y according to $I_y^{\uparrow} = I_{\text{tot}}(1+P_y)/2$ and $I_y^{\downarrow} = I_{\text{tot}}(1-P_y)/2$, where I_{tot} is the spin-averaged intensity. To extract the spin polarization vectors of the forward ($+k_x$) and backward ($-k_x$) moving electrons, we performed a standard numerical fit (SI)²². The fit results yield $100 \pm 15\%$

polarized (see Fig. 1(h)) spins that point along the $\mathbf{k} \times \mathbf{z}$ direction, which is consistent with its spin-orbit coupling origin^{13,22}. Our combined observations of a linear dispersion relation (Figs 1(c) and (d)) and a one-to-one locking of momentum and spin directions allow us to conclude that the surface electrons of $\text{Bi}_2(\text{Se/Te})_3$ are helical Dirac fermions.

To experimentally access these helical Dirac fermions, the electronic structure must be in the topological transport regime. This regime occurs when E_F lies in between the bulk valence band maximum (VBM) and the bulk conduction band minimum (CBM), and exactly at the surface Dirac point, which should in turn lie at a Kramers' time-reversal invariant momentum^{6,20}. This is not the case in either Bi_2Se_3 , graphene or Bi_2Te_3 . Although pure Bi_2X_3 are expected to be undoped semiconductors^{21,23,24}, nominally stoichiometric samples are well known to be *n*- and *p*-type semiconductors due to excess carriers introduced via Se or Te site defects respectively^{15,16}. To compensate for the unwanted defect dopants, trace amounts of carriers of the opposite sign must be added into the naturally occurring material. To lower the E_F of Bi_2Se_3 into the bulk band gap, we substituted trace amounts of Ca^{2+} for Bi^{3+} in as-grown Bi_2Se_3 , where Ca acts as a hole donor¹⁵. Scanning tunnelling microscopy (STM)¹⁵ as well as thermoelectric transport studies¹⁵ suggests that Ca substitution has the additional effect of substantially reducing the number of Se site defects, which also acts to decrease the concentration of excess electron carriers. The topological transport regime is more easily accessed in Bi_2Se_3 compared to Bi_2Te_3 because it has a larger band gap (around 0.35 eV^{25,26} and 0.18 eV^{25,27} respectively) and its surface Dirac point is located much closer in energy to the VBM (Figs 1(c)&(d)). Figure 2(a) shows that as the Ca concentration increases from 0% to 0.25%, there is a dramatic upturn in the low temperature resistivity suggesting a transition from conducting to insulating behaviour. As the Ca concentration increases further to 0.5%, the resistivity drops back down signalling a re-entrance into a conducting regime. The resistivity peak occurs at a Ca concentration where a change in sign of the Hall carrier density also is observed (Fig.

2(b)), which shows that for measured Ca concentrations below and above 0.25%, electrical conduction is supported by electron and hole carriers respectively.

We performed systematic ARPES measurements to study the electronic structure evolution of $\text{Bi}_{2-\delta}\text{Ca}_\delta\text{Se}_3$ as a function of Ca doping in order to gain insight into the trends observed in transport (Figs 2(a) and (b)). Early time (shortly after the cleavage) ARPES energy dispersion maps taken through the $\bar{\Gamma}$ point of the (111) surface Brillouin zone that were collected within 20 minutes of sample cleavage are displayed in Figure 2(c)-(h) for several Ca doping levels. In the as-grown ($\delta = 0$) Bi_2Se_3 samples (Fig. 2(c)), a single surface Dirac cone is observed with E_F lying nearly 0.3 eV above the Dirac node forming an electron Fermi surface (FS). The observation of diffuse intensity near E_F inside the Dirac cone, which comes from a spin-degenerate bulk-surface resonance state at the CBM¹⁴, shows that E_F intersects the electron-like bulk conduction band. When a 0.25% concentration of Ca is introduced, E_F is dramatically lowered to lie near the Dirac node (Fig. 2(d)), which is consistent with Ca acting as a highly effective hole donor. Because the bulk CBM lies at a binding energy of approximately -0.1 eV for $\delta = 0$ (Fig. 2(c)), a 0.3 eV shift in E_F between $\delta = 0$ and $\delta = 0.0025$ suggests that for $\delta = 0.0025$, E_F is located 0.2 eV below the CBM. This is consistent with E_F being in the bulk band gap because the indirect energy gap between the CBM and the VBM is known from both tunneling²⁵ and optical²⁶ data and theory²³ to be nearly 0.35 eV. As the Ca concentration is increased further, the position of E_F continues a downward trend such that by $\delta = 0.01$, it is located clearly below the Dirac node (Fig. 2(e)) and intersects the hole-like bulk valence band. The systematic lowering of E_F with increasing δ in $\text{Bi}_{2-\delta}\text{Ca}_\delta\text{Se}_3$ observed in early time ARPES measurements (Figs 2(i)-(k)), which reflect the electronic structure of the sample bulk, consistently explain the measured transport behaviour. However, we observe that E_F rises back up over time across all samples such that all spectra relax back to a $\delta = 0$ like spectrum on a typical time scale of 18 hours (Fig. 2(l)). Such a slow upward shift of the surface

Fermi level has been observed also in all types of Bi_2Te_3 (SI) and is due to a surface band bending effect commonly observed in most semiconductors¹⁶. Therefore, although bulk Ca doping succeeds in tuning E_F between the bulk valence and conduction bands, it does not change the position of E_F relative to the surface Dirac point in the ground state.

Because the surface Dirac point in the ground state of bulk-insulator $\text{Bi}_{1.9975}\text{Ca}_{0.0025}\text{Se}_3$ lies ~ 0.3 eV below E_F , its electronic structure is still *not* in the much desired topological transport regime. To bring the surface Dirac point level with E_F in $\text{Bi}_{2-\delta}\text{Ca}_\delta\text{Se}_3$, we show that hole carriers can be systematically introduced into the surface by dosing with NO_2 molecules, which has been demonstrated in graphene^{28,29}. Successful molecular adsorption on the (111) surface was confirmed by monitoring changes in the core-level spectral features before and after exposure to NO_2 gas, which provides information about the surface chemical environment (SI). Figure 3 shows that with increasing surface hole donor concentration, the binding energy of the surface Dirac point rises monotonically towards E_F . Starting from $E_B \sim -0.3$ eV at a 0 Langmuir (L) dose (Fig. 3(d)), it rises to -0.15 eV at 0.1 L where the resonance states near the CBM have completely disappeared (Fig. 3(f)), and finally to the charge neutrality point ($E_B = 0$ eV) at 2 L (Fig. 3(i)). No further changes of the chemical potential are observed with higher dosages. To quantify the surface carrier density (n) dependence on surface hole donor concentration, we mapped the surface state FS in Figures 3(a)-(c) and applied Luttinger's theorem $n = A_{\text{FS}}/A_{\text{BZ}}$, where A_{FS} is the area of the FS and A_{BZ} is the area of the surface Brillouin zone. We find that 0.1 L of NO_2 removes approximately 0.0066 electrons per surface unit cell of $\text{Bi}_{2-\delta}\text{Ca}_\delta\text{Se}_3$ (111), and an excess of 2 L reduces the FS to a single point within our experimental resolution, which has an additional 0.005 electrons per unit cell removed. Because surface doping does not affect the carrier density in the bulk, the energy of the Dirac point is lifted above the bulk VBM and a

new time-independent electronic ground state that lies in the topological transport regime is realized for the first time.

In order to demonstrate the thermal stability of nodal Dirac ground state (Fig. 4(e)), temperature dependent ARPES scans were collected on $\text{Bi}_{2-\delta}\text{Ca}_\delta\text{Se}_3$ samples that were first surface hole doped with NO_2 at a temperature $T = 10$ K. Figures 4(c) and (d) illustrate that the charge neutral point-like FS (Fig. 4(a)) is robust up to room temperature ($T = 300$ K) over days long measurement times. An internal consistency check was carried out by systematically studying the temperature dependence of the valence bands (Fig. 4(b)), which shows that the intensity of the NO_2 core level peaks do not change over this temperature range, indicating no measurable NO_2 desorption during the heating process. A density of states that decreases linearly to zero at the Dirac point energy at 300 K (Fig. 4(f)) is further evidence that the low energy properties of $\text{Bi}_{1.9975}\text{Ca}_{0.0025}\text{Se}_3.\text{NO}_2$ are dominated by a novel ground state that features massless helical Dirac fermions.

Helical Dirac fermions are protected from acquiring a mass through band gap formation because they are located around time-reversal invariant (Kramers') momenta $k_T = \bar{\Gamma}$ or \bar{M} (Fig. 4(h))⁶. This makes them fundamentally different from chiral Dirac fermions such as those found in graphene, which are located at \bar{K} and not protected (Fig. 4(g)). The helical Dirac fermion on the surface of Bi_2Se_3 owes its existence to a non-zero bulk topological invariant ν_0 given by $(-1)^{\nu_0} = \prod_{k_T} \prod_{m=1}^N \xi_{2m}(k_T)$, where $\xi_{2m}(k_T)$ is the parity eigenvalue of the bulk wavefunction at the 3D Kramers' point k_T and N is the number of occupied bulk bands²⁰. Because Ca dopants are present in only trace quantities in $\text{Bi}_{1.9975}\text{Ca}_{0.0025}\text{Se}_3.\text{NO}_2$, the values of $\xi_{2m}(k_T)$ do not deviate from those of pure Bi_2Se_3 , as also evidenced by the presence of a single gapless surface band in both Bi_2Se_3 and $\text{Bi}_{1.9975}\text{Ca}_{0.0025}\text{Se}_3$. More importantly, both Ca^{2+} and NO_2^- are non-magnetic

and so do not break time-reversal invariance, therefore the topological protection ($v_0 = 1$) is retained or applies even in the transport regime (Fig. 4(e)), which is stable with both time and temperature. In addition, the remarkable ability to change the sign of the effective helicity $\pm \mathbf{k} \times \mathbf{z}$ (from left-handed to right handed) by tuning the surface chemical potential above or below the surface Kramers' point $\bar{\Gamma}$ (Fig. 4(h)) offers the exciting opportunity to probe interactions between Dirac fermions of opposite helicity at a tuned interface, a long-sought experiment searching for physics beyond the standard model of particle physics³⁰. Condensed matter analogues of such experiments hold promise for realizing novel Bose condensed states of matter¹⁰. In addition, this work paves the way for the realization of half-fermions^{8,9} in condensed matter systems.

1. Day, C. Exotic spin textures show up in diverse materials. *Phys. Today* **62**, 12-13 (2009).
2. Geim, A. K. & Novoselov, K. S. The rise of graphene. *Nature Mat.* **6**, 183-191 (2007).
3. Hsieh, D. *et al.* A topological Dirac insulator in a quantum spin Hall phase. *Nature* **452**, 970-974 (2008).
4. Li, L. *et al.* Phase transitions of Dirac electrons in Bismuth. *Science* **321**, 547-550 (2008).

5. Moore, J. E. & Balents, L. Topological invariants of time-reversal-invariant band structures. *Phys. Rev. B* **75** 121306(R) (2007).
6. Fu, L., Kane, C. L. & Mele, E. J. Topological insulators in three dimensions. *Phys. Rev. Lett.* **98**, 106803 (2007).
7. Qi, X.-L., Hughes, T. L. & Zhang, S.-C. Topological field theory of time-reversal invariant insulators. *Phys. Rev. B* **78**, 195424 (2008).
8. Fu, L. & Kane, C. L. Probing neutral Majorana fermion edge modes with charge transport. Preprint at <<http://arxiv.org/abs/0903.2427>> (2009).
9. Akhmerov, A. R., Nilsson, J. & Beenakker, C. W. J. Electrically detected interferometry of Majorana fermions in a topological insulator. Preprint at <<http://arxiv.org/abs/0903.2196>> (2009).
10. Seradjeh, B., Moore, J. E. & Franz, M. Exciton condensation and charge fractionalization in a topological insulator film. Preprint at <<http://arxiv.org/abs/0902.1147>> (2009).
11. Essin, A., Moore, J. E. & Vanderbilt, D. Magnetoelectric polarizability and axion electrodynamics in crystalline insulators. *Phys. Rev. Lett.* **102**, 146805 (2009).

12. Ran, Y., Zhang, Y. & Vishwanath, A. One-dimensional topologically protected modes in topological insulators with lattice dislocations. *Nature Phys.* **5**, 298-303 (2009).

13. Hsieh, D. *et al.* Observation of unconventional quantum spin textures in **BiSb**-alloy topological insulator. *Science* **323**, 919-922 (2009).

14. Xia, Y. *et al.* Electrons on the surface of Bi_2Se_3 form a topologically-ordered two dimensional gas with a non-trivial Berry's phase. *Nature Phys.* in press. Preprint at <<http://arxiv.org/abs/0812.2078>> (2008).

15. Hor, Y. S. *et al.* p-type Bi_2Se_3 for topological materials and thermoelectric applications. Preprint at <<http://arxiv.org/abs/0903.4406>> (2009).

16. Noh, H.-J. *et al.* Spin-orbit interaction effect in the electronic structure of Bi_2Te_3 observed by angle-resolved photoemission spectroscopy. *Europhys. Lett.* **81**, 57006 (2008).

17. Chen, Y. L. *et al.* Large gap topological insulator Bi_2Te_3 with a single Dirac cone on the surface. Preprint at <<http://arxiv.org/abs/0904.1829>> (2009).

18. Checkelsky, J. G., Li, L. & Ong, N. P. Divergent resistance of the Dirac point in graphene: Evidence for a transition in high magnetic field. *Phys. Rev. B* **79**, 115434 (2009).

19. Franz, M. High energy physics in a new guise. *Physics* **1**, 36 (2008).

20. Fu, L. & Kane, C. L. Topological insulators with inversion symmetry. *Phys. Rev. B.* **76**, 045302 (2007).

21. Zhang, H. *et al.* Topological insulators at room temperature. Preprint at <http://arxiv.org/abs/0812.1622> (2008).

22. Meier, F., Dil, J. H., Lobo-Checa, J., Patthey, L. & Osterwalder, J. Quantitative vectorial spin analysis in angle-resolved photoemission: Bi/Ag(111) and Pb/Ag(111). *Phys. Rev. B* **77**, 165431 (2008).

23. Larson, P. *et al.* Electronic structure of Bi_2X_3 (X = S, Se, T) compounds: Comparison of theoretical (bulk band) calculations with photoemission density-of-states studies. *Phys. Rev. B* **65**, 085108 (2001).

24. Mishra, S. K., Satpathy, S. & Jepsen, O. Electronic structure and thermoelectric properties of bismuth telluride and bismuth selenide. *J. Phys: Condens. Mat.* **9**, 461-470 (1997).

25. Urazhdin, S. *et al.* Surface effects in layered semiconductors Bi_2Se_3 and Bi_2Te_3 . *Phys. Rev. B* **69**, 085313 (2004).

26. Black, J., Conwell, E. M., Seigle, L. & Spencer, C. W. Electrical and optical properties of some $M_2^{V-B}N_3^{VI-B}$ semiconductors. *J. Phys. Chem. Sol.* **2**, 240-251 (1957).

27. Thomas, G. A. *et al.* Large electron-density increase on cooling a layered metal: Doped Bi_2Te_3 . *Phys. Rev. B* **46**, 1553-1556 (1992).

28. Zhou, S., *et al.* A. Metal to insulator transition in epitaxial graphene. *Phys. Rev. Lett.* **101**, 086402 (2008).

29. Schedin, F. *et al.* Detection of individual gas molecules adsorbed on graphene. *Nature Mat.* **6**, 652-655 (2007).

30. Wilczek, F. Remarks on dyons. *Phys. Rev. Lett.* **48**, 1146-1149 (1982).

31. Hsieh, D. *et al.* First observation of spin-helical Dirac fermions and topological phases in undoped and doped Bi_2Te_3 demonstrated by spin-ARPES. Preprint at <<http://arxiv.org/abs/0904.1260>> (April-2009). **Results from this preprint have been completely incorporated into the present single manuscript submitted here.**

Supplementary Information accompanies the paper on www.nature.com/nature.

Correspondence and requests for materials should be addressed to M.Z.H. (mzhasan@princeton.edu).

Figure 1 : Detection of helical Dirac electrons using spin-resolved ARPES.

(a) ARPES intensity map at E_F of the (111) surface of tuned $\text{Bi}_{2-\delta}\text{Ca}_\delta\text{Se}_3$ (see text) and (b) the (111) surface of Bi_2Te_3 . Red arrows denote the direction of spin around the Fermi surface. (c) ARPES dispersion of tuned $\text{Bi}_{2-\delta}\text{Ca}_\delta\text{Se}_3$ and (d) Bi_2Te_3 along the k_x cut. The dotted red lines are guides to the eye. The point marked X in (c) labels the position of the Dirac node in pure Bi_2Se_3 ¹⁴. The shaded regions in (c) and (d) are our calculated projections of the bulk bands of pure Bi_2Se_3 and Bi_2Te_3 onto the (111) surface respectively (SI). (e) Measured y component of spin-polarization along the $\bar{\Gamma} - \bar{M}$ direction at $E_B = -20$ meV, which only cuts through the surface states. The solid line is a numerical fit²². Inset shows a schematic of the cut direction. (f) Measured x (red triangles) and z (black circles) components of spin-polarization along the $\bar{\Gamma} - \bar{M}$ direction at $E_B = -20$ meV. (g) Spin-resolved spectra obtained from the y component spin polarization data. The non-Lorentzian lineshape of the I_y^\uparrow and I_y^\downarrow curves and their non-exact merger at large $|k_x|$ is due to the time evolution of the surface band dispersion, which is the dominant source of statistical uncertainty. (h) Fitted values of the spin polarization vector (P_x, P_y, P_z) are $(\sin(90^\circ)\cos(-95^\circ), \sin(90^\circ)\sin(-95^\circ), \cos(90^\circ))$ for electrons with $+k_x$ and $(\sin(86^\circ)\cos(85^\circ), \sin(86^\circ)\sin(85^\circ), \cos(86^\circ))$ for electrons with $-k_x$, which demonstrates the helicity of the Dirac cone. The angular uncertainties are of order $\pm 10^\circ$ and the magnitude uncertainty is of order ± 0.15 .

Figure 2 : Tuning the bulk Fermi level through systematic charge

compensation. (a) Resistivity at $T = 4$ K measured for samples of Bi_2Se_3 that are bulk electron doped due to varying concentrations of Se vacancies¹⁵ (x) or bulk hole doped through Ca/Bi substitution (δ). These are compared to

analogous values for topological insulators $\text{Bi}_{0.9}\text{Sb}_{0.1}$ ³ and $\text{Bi}_{1.9933}\text{Sn}_{0.0067}\text{Te}_3$ ¹⁷. (b) Hall carrier density of the same samples determined using Hall measurements. Symbols colored red (blue) represent n - (p -) type behavior. (c) ARPES band dispersion images of $\text{Bi}_{2-\delta}\text{Ca}_\delta\text{Se}_3$ (111) through $\bar{\Gamma}$ collected within 20 minutes after cleavage for $\delta = 0$, (d) $\delta = 0.0025$ and (e) $\delta = 0.01$. Panels (f) through (h) show the corresponding momentum distributions curves. Red lines are guides to the eye. Panels (i) through (k) show the schematic downward evolution of E_F with increasing Ca content. The occupied bulk conduction band (BCB) and bulk valence band (BVB) states are shaded dark, and the occupied surface states (SS) are colored red. (l) Typical ARPES band dispersion image of panels (c) through (e) taken around 18 hours after cleavage and (m) its corresponding momentum distribution curves. (n) Schematic of the surface band bending process that is responsible for the observed downward shift in energies over time.

Figure 3: Tuning the density of helical Dirac electrons to the spin-degenerate Kramers' point. (a) A high resolution ARPES mapping of the surface Fermi surface (FS) near $\bar{\Gamma}$ of $\text{Bi}_{2-\delta}\text{Ca}_\delta\text{Se}_3$ (111). The diffuse intensity within the ring originates from the surface resonance state. (b) The FS after 0.1 Langmuir (L) of NO_2 is dosed, showing that the resonance state is removed. (c) The FS after a 2 L dosage, which achieves the Dirac charge neutrality point. (d) High resolution ARPES surface band dispersions through $\bar{\Gamma}$ after an NO_2 dosage of 0 L, (e) 0.01 L, (f) 0.1 L, (g) 0.5 L, (h) 1 L and (i) 2 L. The arrows denote the spin polarization of the bands. We note that due to an increasing level of surface disorder with NO_2 adsorption, the measured spectra become

progressively more diffuse and the total photoemission intensity from the buried $\text{Bi}_{2-\delta}\text{Ca}_\delta\text{Se}_3$ is reduced.

Figure 4 : Thermal stability of the nodal helical Dirac ground state. (a)

Typical ARPES intensity map of the $\text{Bi}_2(\text{Se/Te})_3$ class collected at E_F spanning several Brillouin zones. (b) Energy distribution curves of the valence bands of $\text{Bi}_{2-\delta}\text{Ca}_\delta\text{Se}_3$ taken at $T = 10$ K, 200 K and 300 K. The peaks around -4 eV and -7.5 eV come from NO_2 adsorption (SI). (c) ARPES intensity map of the surface state band dispersion of $\text{Bi}_{2-\delta}\text{Ca}_\delta\text{Se}_3$ (111) after a 2 L dosage of NO_2 is applied at $T = 10$ K, which is taken at 300 K and (d) 10 K. (e) Schematic of the surface and bulk electronic structure of $\text{Bi}_{2-\delta}\text{Ca}_\delta\text{Se}_3.\text{NO}_2$, tuned to the topological transport regime. (f) Angle-integrated intensity near $\bar{\Gamma}$ (red) shows a linear trend. The inset shows the expected density of states (DOS) of a helical Dirac cone, which is 1/2 that of a graphene Dirac cone due to its single spin degeneracy. (g) Schematic of the chiral Dirac fermion ground state of graphene, which exhibits spin-degenerate Dirac cones that intersect away from the Kramers' points. (h) Schematic of the helical Dirac fermion ground state of $\text{Bi}_{2-\delta}\text{Ca}_\delta\text{Se}_3.\text{NO}_2$, which exhibits a spin-polarized Dirac cone that intersects at a Kramers' point and guarantees a non-zero topological quantum number for the helical ground state.

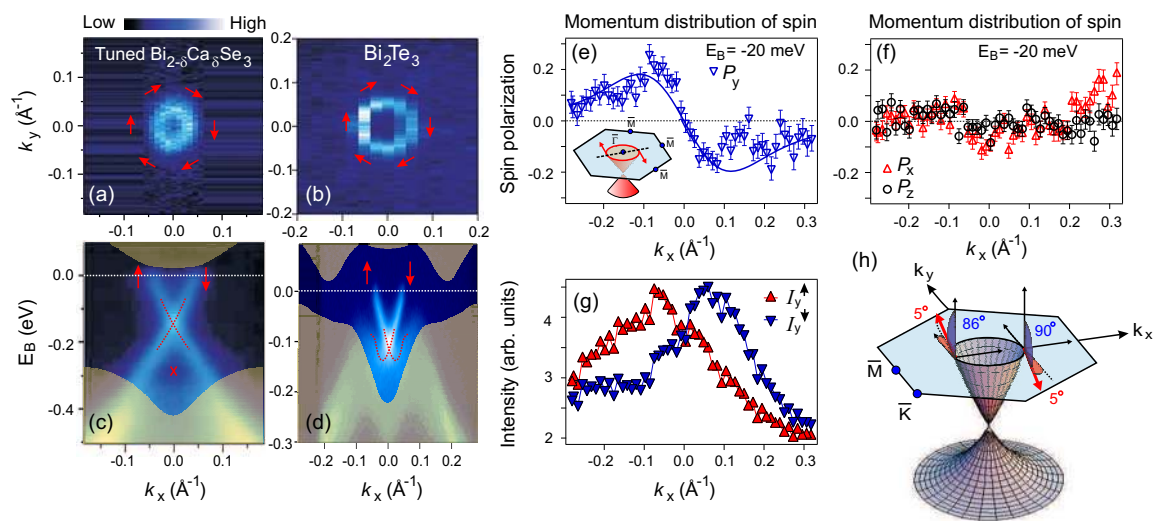


FIG. 1: M.Z. Hasan

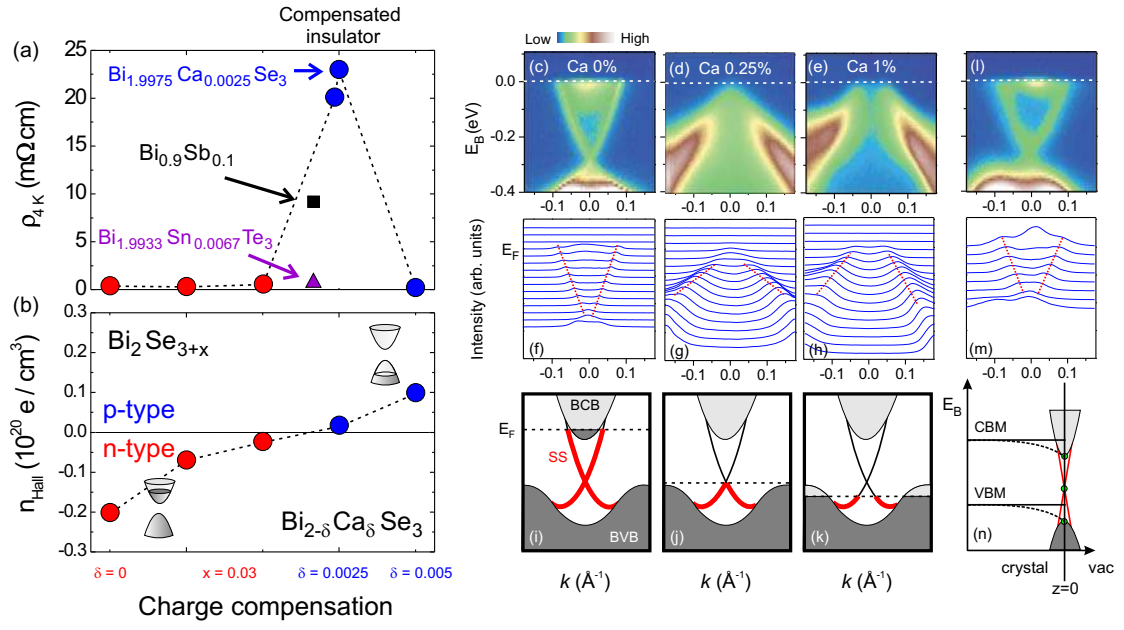


FIG. 2: M.Z. Hasan

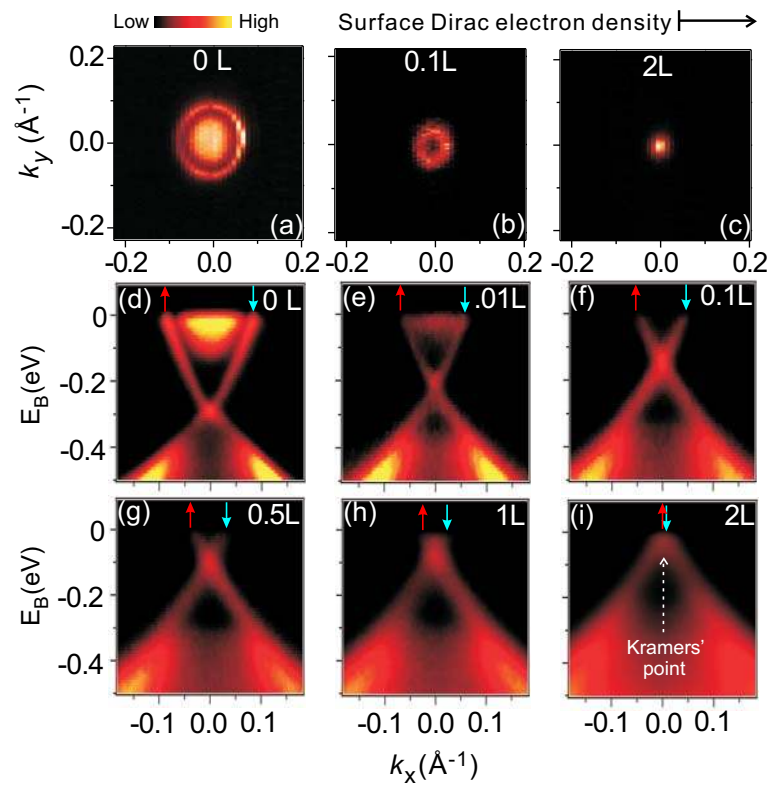


FIG. 3: M.Z. Hasan

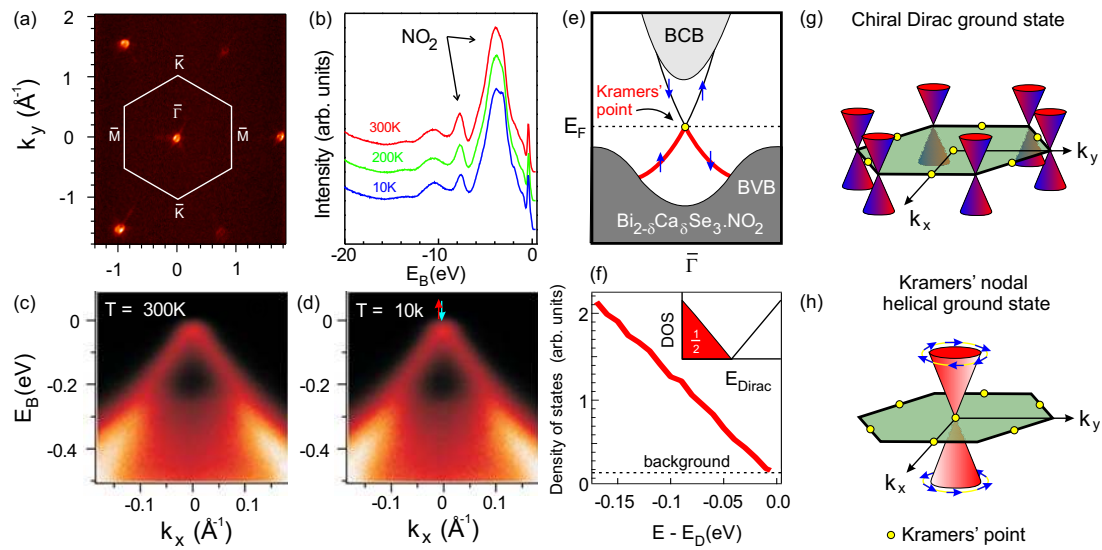


FIG. 4: M.Z. Hasan